



# Ultralong-life lithium metal batteries enabled by decorating robust hybrid interphases on 3D layered frameworks



Qiongjie Ke<sup>a</sup>, Qingshuai Xu<sup>a</sup>, Xuejun Lai<sup>a</sup>, Xianfeng Yang<sup>a</sup>, Huichun Gao<sup>b</sup>,  
Zaisheng Wang<sup>a,\*</sup>, Yongcai Qiu<sup>a,\*</sup>

<sup>a</sup>School of Environment and Energy, State Key Laboratory of Luminescent Materials and Device, Guangdong Provincial Key Laboratory of Atmospheric Environment and Pollution Control, South China University of Technology, Guangzhou 510000, China

<sup>b</sup>EVE Energy Co., Ltd., Huizhou 516000, China

## ARTICLE INFO

### Article history:

Received 9 May 2022

Revised 25 May 2022

Accepted 8 June 2022

Available online 16 June 2022

### Keywords:

Lithium metal battery

TiF<sub>4</sub>

Artificial SEI

Dendrite free

3D frameworks

## ABSTRACT

Stable solid-electrolyte interphase (SEI) is crucial for advanced development of lithium metal batteries. However, the continuous collapse and reconstruction of SEI will deplete fresh Li and electrolytes upon cycling, leading to irreversible capacity loss. Herein, we addressed this issue by pre-formation of artificial robust hybrid interphase on a 3D layered graphene/lithium metal framework, in which is constructed by LiF associated with Li<sub>2</sub>TiF<sub>6</sub> generated by the *in-situ* reaction between the surficial lithium and titanium fluoride contained electrolytes. The as-obtained interphase can maintain the structure integrity and avoid continuous consumption of the fresh Li and electrolytes. As a consequence, the Li symmetric cells achieve high-efficiency Li deposition and stable cycling over 3600 h. When paired with LiFePO<sub>4</sub> cathodes, the coin cells exhibit long lifespan (>800 cycles) with almost 88.3% retention of the initial capacity.

© 2023 Published by Elsevier B.V. on behalf of Chinese Chemical Society and Institute of Materia Medica, Chinese Academy of Medical Sciences.

Lithium (Li) metal has been considered as a promising anode material for future high energy batteries in portable electronics and electric vehicles owing to its high theoretical capacity and the lowest anode potential [1–4]. In Li metal batteries, constructing stable solid-electrolyte interphase (SEI) is among the most effective strategies to prevent the Li dendrite growth and thus to improve the cycling efficiency. The SEI layer is a passivation film with a complicated and heterogeneous sub-structure [5,6], which consists of reduction products formed through the reactions between Li anodes and electrolytes [7,8]. However, the natural SEI layer derived from the electrolyte decomposition is mechanically unstable under electrochemical process. Inflexible and fragile SEI cannot bear the huge interfacial fluctuations and morphological changes of Li anode upon cycling [9–12], as a sequence of low Coulombic efficiency and poor cycle lifetime [13]. Meanwhile, large Li dendrites forming due to the inhomogeneous Li deposition further causes short-circuit of the battery [14–17].

Considerable efforts have been made to develop various strategies for stabilizing the SEI, homogenizing Li deposition, and tackling dendrite formation [18]. Current strategies employed to accomplish those purposes can be specifically divided into three

categories: (1) Engineering stable SEI [19–22]; (2) Designing “host” structures to accommodate the Li metal and withstand the volume fluctuation [23–27]; (3) Using solid electrolyte to inhibit the dendrite formation [28–30]. These methodologies are effective to a certain extent for mitigating either or both dendritic Li growth and SEI destruction. Nevertheless, none of them can address the continuous fracture and reconstruction of the SEI layer in term of the huge volume fluctuation during cycling. Therefore, developing a new approach capable of solving these multifaceted problems is imperative.

Theoretically, combining an artificial robust interphase with a host framework can conquer the interrelated intrinsic problems: the instable SEI and dendritic Li formation, and volume change during cycling. Recently, a 3D layered framework with numerous nanogaps has exhibited improved Li plating/stripping performance, in which Li can deposit into the nanogaps between reduced graphene oxide (rGO) sheets [31]. Despite the superiority of nanogaps for suppressing the dendritic Li growth, the natural SEI layer that is mechanically not strong enough to sustain the huge interfacial fluctuation, ultimately causing the irreversible capacity loss due to the continuous breakdown and reformation of SEI.

Titanium-based compounds have been widely used as energy storage materials due to their excellent chemical performance [32]. Lithium-hexafluoro-titanium (Li<sub>2</sub>TiF<sub>6</sub>) as a lithium ionic conductive

\* Corresponding authors.

E-mail addresses: 842700923@qq.com (Z. Wang), ycqiu@scut.edu.cn (Y. Qiu).

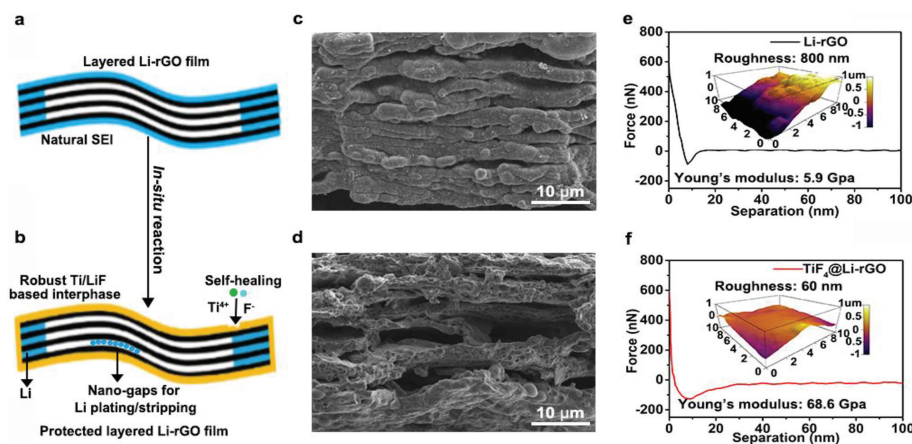


**Fig. 1.** Schematic illustration of the *in-situ* process and physical characterization of the  $\text{TiF}_4\text{@Li-rGO}$  electrode. Schematic illustration of the (a) Li-rGO and (b)  $\text{TiF}_4\text{@Li-rGO}$ . Cross-sectional view of the (c) Li-rGO and (d)  $\text{TiF}_4\text{@Li-rGO}$  electrode. The contrast stress force-distance curves of (e) Li-rGO and (f)  $\text{TiF}_4\text{@Li-rGO}$  electrodes. The corresponding three-dimensional AFM scanning images of the surface for the different electrodes are shown as insets.

material simultaneously possesses high conductivity and mechanical strength [33]. To solve the mechanical and chemical unstable characteristic of the natural SEI (Fig. 1a), we propose to introduce  $\text{Li}_2\text{TiF}_6$  into the natural SEI for improving its mechanical strength, but do not lower its ionic conductivity considerably. Here, we fabricate a 3D layered structure by immersing 3D layered Li-rGO framework into  $\text{TiF}_4$ -containing electrolyte. The *in-situ* chemical reaction generates  $\text{Li}_2\text{TiF}_6$  which then associates with LiF to form a robust hybrid solid interphase on Li-rGO (Fig. 1). The 3D-structured electrode (denoted as  $\text{TiF}_4\text{@Li-rGO}$ ) shows remarkable cycling stability with ultralong lifespan (ten times higher than the pristine Li-rGO electrode) in symmetric cells and has improved capacity retention (>800 cycles with almost 88.3% retention of the initial capacity) when paired with  $\text{LiFePO}_4$  (LFP) cathode.

The synthesis process of the  $\text{TiF}_4\text{@Li-rGO}$  electrode can be divided into three steps. Firstly, highly concentrated GO solution (5 mg/mL) was used to obtain freestanding GO films by vacuum filtration, zinc fluoride ( $\text{ZnF}_2$ , anhydrous, 99%, Aladdin) was used as additive (1:1, w/w) in the GO solution to make the vacuum filtration more fluent. According to our previous work, the small addition of  $\text{ZnF}_2$  that aimed to make the filtration easier can be removed with filtrate and has little effect on the electrochemical performance [34]. After filtration, collected films were first dried in a vacuum oven at 60 °C overnight, tailored into small round pieces (~14 mm), then contacted with stainless steel at a high temperature of 350 °C to gain highly lithiophilic rGO film. After cooling down to room temperature, the Li-rGO was immersed into a supersaturated as-prepared solution using titanium tetrafluoride ( $\text{TiF}_4$ , metal basis, 99.9%) as additive (10 wt%  $\text{TiF}_4$  in EC-EMC-DEC, 3:5:2, w/w) for 10 min, the color of the Li-rGO changes from khaki to black. The as-obtained  $\text{TiF}_4\text{@Li-rGO}$  films were collected after washing with anhydrous DEC three times. All lithium metal and electrolyte contained experiment were carried out in an argon-filled glove box (Vigor, China,  $\text{O}_2$  and  $\text{H}_2\text{O}$  content < 0.1 ppm). The as-prepared samples characterization and electrochemical measurements are attached in Supporting information.

The cross-sectional SEM images for Li-rGO and  $\text{TiF}_4\text{@Li-rGO}$  electrode were shown in Figs. 1c and d. It is noted that large inter-spaces between these layered Li-rGO units are observed (Fig. 1c), which allows the electrolytes to access the units, thereby significantly increasing the surface area for electrochemical reactions. After immersing the Li-rGO film into the  $\text{TiF}_4$  contained electrolyte, the color of Li-rGO anode changes from khaki to black within minutes (Fig. S1 in Supporting information). The *in-situ* chemical reaction occurs between Li-rGO and  $\text{TiF}_4$ , forming a  $\text{Li}_2\text{TiF}_6/\text{LiF}$

based SEI on Li-rGO (Fig. 1d and Fig. S2 in Supporting information). The hybrid SEI is expected to be an excellent lithium-ion conductor [35,36]. As verified by X-ray diffraction (XRD), the peaks at  $2\theta = 21.6^\circ$ ,  $27.2^\circ$  and  $40.9^\circ$  correspond to (101), (110) and (113) planes of  $\text{Li}_2\text{TiF}_6$ , respectively, and the peaks at  $2\theta = 38.7^\circ$ ,  $44.9^\circ$  and  $65.4^\circ$  correspond to (111), (200) and (220) planes of LiF, respectively (Fig. S3 in Supporting information) [37,38]. The SEI compositions were further investigated by in-depth X-ray photoelectron spectroscopy (XPS). As shown in Fig. S4 (Supporting information), in the case of the Ti 2p spectra, the peak of Ti 2p at 458.8 eV indicates the formation of  $\text{Li}_2\text{TiF}_6$  associated with the peak of F 1s at 687.0 eV, whereas the peak at 464.5 eV shows the present of  $\text{TiF}_3$ . The peaks of F 1s at 684.9 eV and Li 1s at 55.8 eV are assigned to LiF. Moreover, the peak of Li 1s at 54.6 eV corresponds to metallic Li. The energy dispersive spectroscopy (EDS) elemental mapping shows that F and Ti are homogeneously distributed on the SEI, and the chemical composition of the cross-sectional side and top surface of the electrode are similar (Figs. S5–S7 in Supporting information). Thus, the  $\text{Li}_2\text{TiF}_6$  and LiF are chemically bounded into the artificial solid-state interphase on the exterior of layered Li-rGO units.

The retracted force-distance curve collected by atomic force microscope (AFM) shows a great leap that the Young's modulus value of hybrid solid-state interphase (68.6 GPa) is ten times stronger than the routine SEI on Li metal (5.9 GPa) (Figs. 1e and f), which transcends the threshold modulus value for suppressing Li-dendrite growth [39]. Such high-strength SEIs can suppress Li dendrites and conquer the huge volume fluctuation which further triggers repeated SEI collapse and reconstruction during cycling. Besides, the surface of the hybrid electrode is much smoother compared to the pristine Li-rGO. Therefore, the formed robust interphase not only can reduce the direct exposure of Li anode to electrolyte, but also can effectively prevent the short-circuit due to the damage of Li dendrites which triggers safety issues in a practical battery.

To account for the specific mechanism of the strategy we propose, galvanostatic charge/discharge test in symmetric cell was first compared between Li foil and  $\text{TiF}_4\text{@Li}$  foil (Fig. S8 in Supporting information). The overpotentials of both Li foil and  $\text{TiF}_4\text{@Li}$  foil steadily increase to 750 mV after 250 h, indicating that the planar SEI layer on Li foil still cannot bear the huge volume change due to the hostless nature (1 mAh corresponding to  $5\ \mu\text{m}$  volume change).

We further compare the voltage profiles of symmetric cells based on 3D layered  $\text{TiF}_4\text{@Li-rGO}$  electrodes and Li-rGO electrodes.

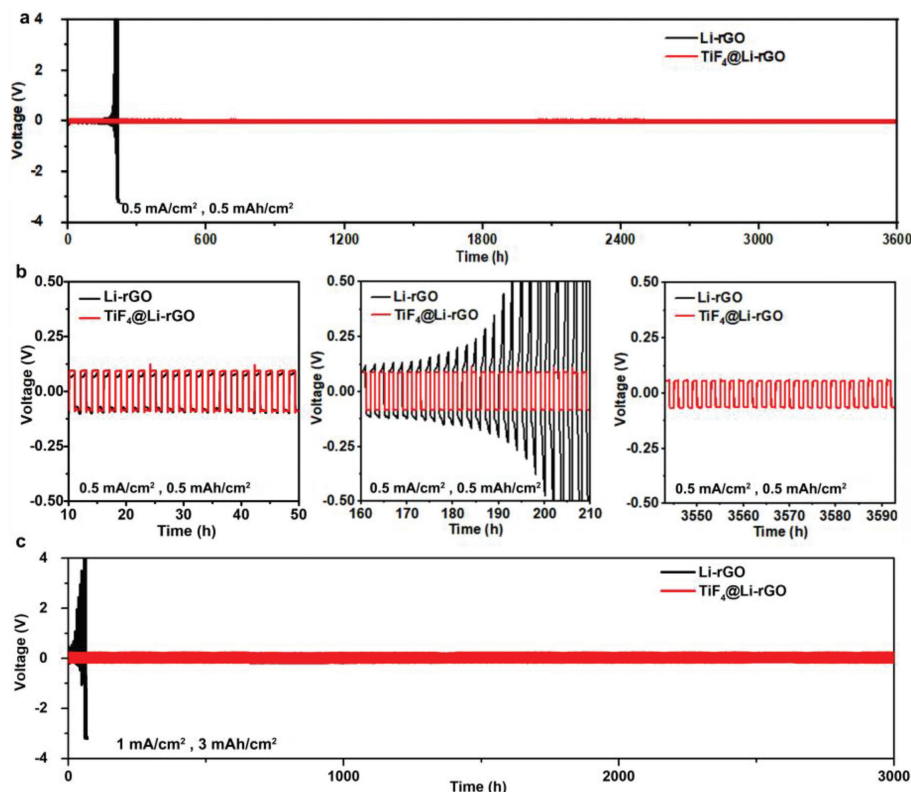


**Fig. 2.** Electrochemical characterizations of the symmetric cells for Li stripping/plating. Galvanostatic cycling of symmetric Li-rGO anode (black) and  $\text{TiF}_4$ @Li-rGO anode (red) with current density fixed at (a)  $0.5 \text{ mA/cm}^2$  and stripping/plating capacity of  $0.5 \text{ mAh/cm}^2$ , and (b) corresponding enlarged view of voltage profiles at different cycles. (c) Cycling stability test with current density fixed at  $1 \text{ mA/cm}^2$  and stripping/plating capacity of  $3 \text{ mAh/cm}^2$ .

It should be noted that there are large voltage fluctuations in the initial several cycles for  $\text{TiF}_4$ @Li-rGO based cells (Fig. S9a in Supporting information), which may be due to the hybrid SEI within the internal electrode is gradually forming and the initial ionic conductivity of the SEI is not good. As shown in Fig. S10 (Supporting information). The impedance of the cell significantly decreases through electro-chemical cycling activation for more than ten hours, which is likely due to the re-organization of the hybrid SEI layer (as will be explained below). After that, the symmetric cell shows long term cycling stability (Fig. S9b in Supporting information).

The symmetric cells also were investigated with current density fixed at  $0.5 \text{ mA/cm}^2$  and a capacity of  $0.5 \text{ mAh/cm}^2$  (Fig. 2a). As seen, it shows extraordinary long term cycling stability over 3600 h and maintains a relatively low overpotential of 90 mV (Fig. 2b). Furthermore, the cells with an increased areal density of  $3 \text{ mAh/cm}^2$  at  $1 \text{ mA/cm}^2$  were also employed to test the cycling stability. As seen in Fig. 2c, the cell undergoes a stable cycling over 3000 h with stable hysteresis. Remarkably, the cycling stability of  $\text{TiF}_4$ @Li-rGO based cells under different testing conditions is much better than Li-rGO counterparts (only has stable cycling around 200 h). The magnified voltage profiles of the selected cycles (Figs. S11a–c in Supporting information) further indicate the stable cycling of  $\text{TiF}_4$ @Li-rGO based cells with flat voltage plateau throughout the cycles. Additionally, the voltage profiles comparison between Li-rGO and  $\text{TiF}_4$ @Li-rGO symmetric cell under various current densities and areal capacity are also shown in Figs. S12 and S13 (Supporting information), respectively. Continuous flat charging and discharging plateaus can be observed under all applied current densities and areal capacities for the  $\text{TiF}_4$ @Li-rGO based cells, suggesting its capability of working under all applied current densities and areal capacities for varied purposes.

To gain further insight into the mechanism of how the  $\text{TiF}_4$ @Li-rGO based cells achieve long-term cycling stability, high-resolution TEM was used to investigate the detailed structure of SEI before and after cyclic activation. We observe that the SEI structure is no longer an irregular distribution of organic and inorganic compound reported previously after reacting the layered Li-rGO unit with  $\text{TiF}_4$  contained electrolytes [40], the SEI possesses ultrafine crystals across the layered Li-rGO unit (Fig. 3a and Fig. S14 in Supporting information), the as-formed SEI layer mainly contains  $\text{Li}_2\text{TiF}_6$ , LiF,  $\text{TiF}_3$ ,  $\text{Li}_2\text{O}$  and  $\text{Li}_2\text{CO}_3$ , as confirmed by EDS mapping and selected area electron diffraction (Figs. 3b and c). The  $\text{Li}_2\text{O}$  and  $\text{Li}_2\text{CO}_3$  mainly come from the decomposition of carbonate electrolyte, which can be assigned to the thermo-dynamic instability of Li anode against carbonate molecules [41]. After electrochemical activation, it is noted that the hybrid SEI is reorganized and a thin layer amorphous matrix forms on the hybrid interphase, which can be derived from the electrolyte decomposition (Figs. 3d–f). Despite a slightly decreased value (25.6 GPa) of Young's modulus (Fig. S15 in Supporting information), the reconstructed SEI greatly facilitates the Li-ion migration through the interphase, in agreement with the cycling performance and EIS tests (Figs. S9 and S10). Therefore, we believe that the preformed robust interphase and additional  $\text{TiF}_4$  additive play a crucial role in forming the final stable SEI, whose structure should be more ordered owing to the introduction of  $\text{Li}_2\text{TiF}_6$ . It has been reported that the ordered nature of a hybrid structure can provide enhanced mechanical durability, making it more robust upon cycling [42].

To understand the feature of nanogaps between  $\text{TiF}_4$ @Li-rGO, we used *in-situ* TEM to observe the Li plating/stripping processes. Two electrodes (Li metal and  $\text{TiF}_4$ @Li-rGO electrodes) are separated by natively formed Li oxide/nitride on Li metal as the electrolyte (Fig. 3g). When an appropriate bias was applied across the

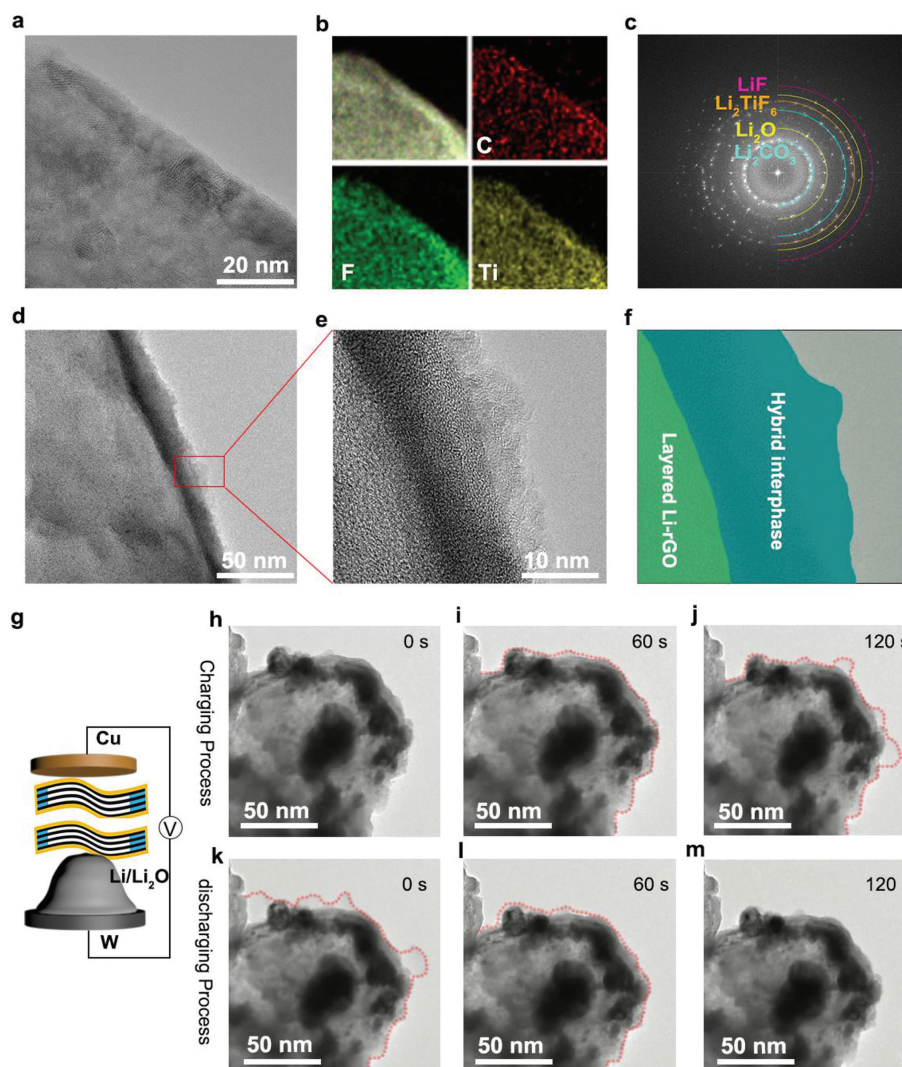


**Fig. 3.** *Ex-situ* and *in-situ* TEM characterization of the hybrid interphase for 3D layered  $\text{TiF}_4@Li\text{-rGO}$  electrode. (a) HRTEM image of the hybrid interphase for  $\text{TiF}_4@Li\text{-rGO}$  electrode before activation. (b) Composition analysis of the hybrid interphase for  $\text{TiF}_4@Li\text{-rGO}$  by energy-dispersive X-ray spectroscopy mapping. (c) SAED (selected area electron diffraction) of the hybrid interphase for  $\text{TiF}_4@Li\text{-rGO}$ . (d) TEM image of the hybrid interphase for  $\text{TiF}_4@Li\text{-rGO}$  electrode after activation at low magnifications. (e) HRTEM image of the hybrid interphase for  $\text{TiF}_4@Li\text{-rGO}$  electrode after activation. (f) Schematics of the observed hybrid interphase structure on  $\text{TiF}_4@Li\text{-rGO}$ . (g) Scheme of *in-situ* TEM cell configuration. *In-situ* TEM images of the Li (h–j) charging and (k–m) discharging process on Cu grid decorated with nano-level  $\text{TiF}_4@Li\text{-rGO}$  taken at different times.

two electrodes, Li ions began to flow into the  $\text{TiF}_4@Li\text{-rGO}$  electrode. Video S1 (Supporting information) presents such a plating process clearly and selected snapshots along the timeline are presented in Figs. 3h–j. At first, the lithium ions traversed the hybrid interphase and homogeneously deposited into the nanogaps. After the nanogaps were filled up with lithium, the lithium ions then deposited on the outside of the unit. Obviously, the robust hybrid interphase maintains its original appearance during the whole charging process. The lithium plating process is reversible, as presented in Video S2 (Supporting information). When the lithium was stripped out from the nanogaps, the outside lithium was first stripped and then the inner lithium was extracted (Figs. 3k–m). During the charging and discharging processes, the layered  $\text{TiF}_4@Li\text{-rGO}$  unit was well protected without obvious volume change. Such unique structure can significantly improve the stability of Li metal anode as the direct exposure of Li metal to electrolyte is prevented.

The liquid cell has been established for visualizing the evolution of lithium metal anodes during the charging and discharging process using operando optical microscopy. The proof-of-principle

of the method directly characterizes electrochemical process under realistic conditions. Figs. 4a and b were taken at discrete time points separated by a fixed 3-min interval. It is observed that the Li foil electrode is prone to forming a moss-like dendritic structure. In comparison, the  $\text{TiF}_4@Li\text{-rGO}$  electrode did not form the dendritic structure. Furthermore, it is seen that the overall volume maintained the same level. Optical observation of each electrode at different plating and stripping cycles was shown in Figs. 4c and d. As seen, once the process initiated, the surfaces of Li electrode became rough, and protrusions started to appear along the edge of the Li electrode. With the cycle proceeding, the protrusions gradually grew up and aggregated to form moss-like dendrites. After 10 cycles, the repeated process could produce a porous Li metal. In contrast, the surface of  $\text{TiF}_4@Li\text{-rGO}$  electrode maintained smooth with no sign of protrusions upon cycling.

The demonstrated strategy significantly enhances the Coulombic efficiency (CE) of Li metal anodes and meets the demand of high-efficiency rechargeable batteries. Here, Aurbach CE test was used to obtain an accurate determination of CE between  $\text{TiF}_4@Li\text{-rGO}$  and Li-rGO [43]. As shown in Fig. 5a, the cell with  $\text{TiF}_4@Li\text{-rGO}$

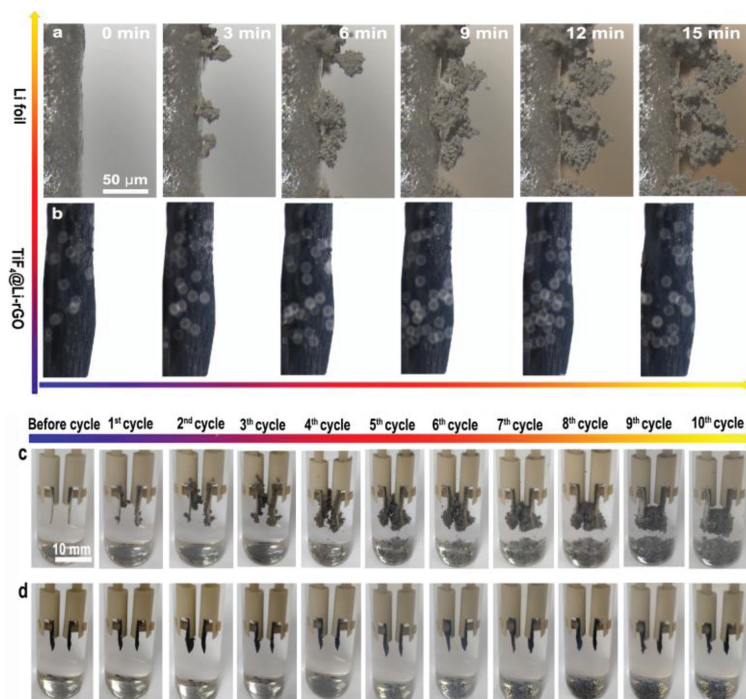


**Fig. 4.** Optical microscopy studies of lithium metal anodes during cycling at a current density of 2 mA/cm<sup>2</sup>. *In-situ* investigation of Li-ion plating behavior with (a) Li foil and (b) TiF<sub>4</sub>@Li-rGO during continuous plating on corresponding electrodes. Electrode surface morphology evolution images of the front surfaces of the (c) Li foil and (d) TiF<sub>4</sub>@Li-rGO electrode in the symmetric transparent cell.

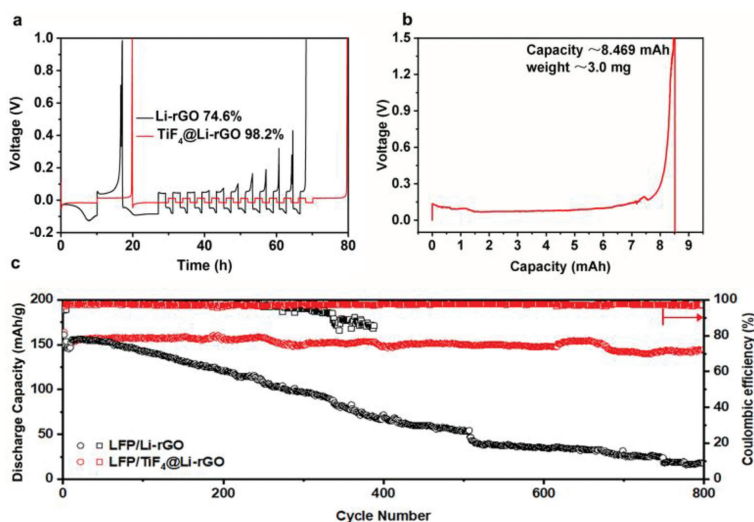


**Fig. 5.** Electrochemical performance of TiF<sub>4</sub>@Li-rGO electrodes. (a) Aurbach measurement of the coulombic efficiency for the TiF<sub>4</sub>@Li-rGO and Li-rGO electrodes (b) Full Li stripping curve of the TiF<sub>4</sub>@Li-rGO electrode to 1.5 V versus Li<sup>+</sup>/Li, which shows a specific capacity of ~2823.0 mAh/g. (c) Performance of full cell comparison between LFP/Li-rGO and LFP/TiF<sub>4</sub>@Li-rGO cells.

rGO achieves a high CE of 98.2%, while the CE for the cell with Li-rGO is just 74.6%. Additionally, after stripping Li metal from the TiF<sub>4</sub>@Li-rGO composite electrode to 1.5 V at a fixed current density of 0.5 mA/cm<sup>2</sup>, the voltage profile shows a total capacity of 8.469 mAh. Therefore, the total specific capacity can be calculated by dividing total capacity by the weight of proposed matrix and the result is 2823.0 mAh/g, which is very close to the theoretical capacity of pristine Li (Fig. 5b). High CE means the great potential for full batteries. When paired with LiFePO<sub>4</sub> (LFP) based full batteries, the LFP/TiF<sub>4</sub>@Li-rGO cell presented a stable cycling performance and delivered a specific capacity of 144.8 mAh/g (with capacity retention of 88.3%) after 800 cycles. On the contrary, the LFP/Li-rGO full cell can only deliver a low specific capacity of 17.7 mAh/g (with

capacity retention of 11.0%) under the same condition (Fig. 5c). Notably, LFP/TiF<sub>4</sub>@Li-rGO cell with high mass loading shows poor cycling performance (with capacity retention of 79.3% after 200 cycles, as shown in Fig. S16 in Supporting information), which is due to that the voids between rGO layers are not large enough to deposit more Li, as verified by *in situ* TEM experiment above. The superior discharge capacity in long-term cycling demonstrates that constructing a unique architecture is an effective way to enhance cycling stability. The relevant experimental results (Figs. S17 and S18 in Supporting information) further demonstrate the robust SEI on the 3D layered Li-rGO anode. The as-formed 3D hybrid interphase on Li-rGO has excellent passivation, homogeneity, and mechanical strength, which can inhibit the dendritic formation and

tolerate the huge interface fluctuation, thus effectively preventing the continuous depletion of electrolyte and fresh Li.

To further investigate the influence of  $\text{TiF}_4$  on the LFP based full cells, an extra experiment was carried out by using different amount of  $\text{TiF}_4$  as an additive in the electrolyte. We firstly measured the cycling stability for each cell. As shown in Fig. S19 (Supporting information), the cell with 1 wt%  $\text{TiF}_4$  additive can deliver a specific capacity of 161 mAh/g at 200<sup>th</sup> cycle (with CE of 97.9%), but the specific capacity for cells with 3 wt%  $\text{TiF}_4$  additive and 5 wt%  $\text{TiF}_4$  additive decreases to 147 mAh/g (with CE of 95.8%) and 130 mAh/g (with CE of 87.7%) at 200<sup>th</sup> cycle, respectively. The cycling profile displays a fast capacity declining rate with the increasing content of  $\text{TiF}_4$  additive and a sharp drop of CE is observed when the concentration is increased to 5 wt%  $\text{TiF}_4$ , indicating that excessive amount of  $\text{TiF}_4$  is harmful for the LFP cathode. SEM and TEM EDS mapping of the LFP cathode after cycling were performed to explain the circumstance (Figs. S20 and S21 in Supporting information). As seen, the surface of LFP covers Ti and F, which can be contributed to  $\text{Li}_x\text{TiF}_{4+x}$  deposition. The deposition would become thicker and thicker upon cycling, resulting in the impediment of  $\text{Li}^+$  transport and the consumption of Li ions.

In conclusion, we report a new architecture of *in-situ* preformed artificial robust hybrid interphase associated with 3D layered Li-rGO framework, which exhibits high-efficiency Li deposition and long-term cycling performance after activation. The as-obtained SEI has outstanding mechanical strength, homogeneity, and passivation properties which outperforms the conventional electrolyte-derived SEI. The resulting anode enables stable cycling of Li symmetric cells over 3600 h. The modified anode based full cells exhibit outstanding cycling performance and high Coulombic efficiency as well. The proposed strategy opens up a promising avenue for promoting the practical applications of lithium metal batteries.

#### Declaration of competing interest

The authors declare that they have no known competing financial interests or personal relationships that could have appeared to influence the work reported in this paper.

#### Acknowledgments

This work is supported by the National Key Research and Development Program of China (No. 2018YFA0209600); Science and Technology Key Project of Guangdong Province, China (No. 2020B010188002); Guangdong Innovative and Entrepreneurial Research Team Program (No. 2019ZT08L075); Foshan Innovative and Entrepreneurial Research Team Program (No. 2018IT100031);

Guangdong Pearl River Talent Program (No. 2019QN01L054); National Natural Science Foundation of China (No. 22176063) and the Fundamental Research Funds for the Central Universities (No. 2020ZYGXZR061).

#### Supplementary materials

Supplementary material associated with this article can be found, in the online version, at doi:10.1016/j.ccl.2022.06.025.

#### References

- [1] M.S. Whittingham, IEEE 100 (2012) 1518–1534.
- [2] S. Chu, A. Majumdar, Nature 488 (2012) 294–303.
- [3] J.M. Tarascon, M. Armand, Nature 414 (2001) 359–367.
- [4] X. Shen, H. Liu, C. Yan, Energy Storage Mater. 12 (2018) 161–175.
- [5] D. Aurbach, J. Power Sources 89 (2000) 206–218.
- [6] E. Peled, S. Menkin, J. Electrochem. Soc. 164 (2017) 1703–1719.
- [7] K. Xu, Chem. Rev. 104 (2004) 4303–4417.
- [8] K. Xu, Chem. Rev. 114 (2014) 11503–11618.
- [9] H. Wang, Y. Li, Nano Lett. 19 (2019) 1326–1335.
- [10] Y. Gao, Z. Yan, J.L. Gray, Nat. Mater. 18 (2019) 384–389.
- [11] J. Wang, H. Wang, J. Xie, Energy Storage Mater. 14 (2018) 345–350.
- [12] X. Shen, R. Zhang, Chen X, et al., Adv. Energy Mater. 10 (2020) 1903645.
- [13] G. Zheng, S.W. Lee, Z. Liang, Natue Nanotech. 9 (2014) 618–623.
- [14] X.B. Cheng, C. Yan, J.Q. Huang, Energy Storage Mater. 6 (2017) 18–25.
- [15] S. Chandrashekar, N.M. Trease, H.J. Chang, Nat. Mater. 11 (2012) 311–315.
- [16] R. Bhattacharyya, B. Key, H. Chen, Nat. Mater. 9 (2010) 504–510.
- [17] J.F. Ding, R. Xu, C. Yan, et al., J. Energy Chem. 59 (2021) 306–319.
- [18] Y. Lu, Z. Tu, L.A. Archer, Nat. Mater. 13 (2014) 961–969.
- [19] C.Z. Zhao, X.B. Cheng, R. Zhang, Energy Storage Mater. 3 (2016) 77–84.
- [20] Y. Liu, Q. Liu, L. Xin, Nat. Energy 2 (2017) 17093.
- [21] M.S. Kim, J.H. Ryu, Deepika, Nat. Energy 3 (2018) 889–898.
- [22] R. Xu, X.B. Cheng, C. Yuan, Matter 1 (2019) 317–344.
- [23] B. Hong, H. Fan, X.B. Cheng, Energy Storage Mater. 16 (2019) 259–266.
- [24] L.L. Lu, Y. Zhang, Z. Pan, Energy Storage Mater. 9 (2017) 31–38.
- [25] Y.G. Lee, S. Fujiki, C. Jung, Nat. Energy 5 (2020) 299–308.
- [26] G. Li, Z. Liu, Q. Huang, Nat. Energy 3 (2018) 1076–1083.
- [27] L. Wang, Z. Zhou, X. Yan, Energy Storage Mater. 14 (2018) 22–48.
- [28] N. Kamaya, K. Homma, Y. Yamakawa, Nat. Mater. 10 (2011) 682–686.
- [29] Y. Kato, S. Hori, T. Saito, Nat. Energy 1 (2016) 16030.
- [30] R. Bouchet, S. Maria, R. Meziane, Nat. Mater. 12 (2013) 452–457.
- [31] D. Lin, Y. Liu, Z. Liang, Nat. Nanotech. 11 (2016) 626–632.
- [32] S. Wang, W. Quan, Z. Zhu, et al., Nat. Commun. 8 (2017) 627.
- [33] M.K. Kim, J. Kim, S.H. Yu, J. Mun, Y.E. Sung, J. Electrochem. Soc. 10 (2019) 223–230.
- [34] Q. Xu, X. Yang, M. Rao, et al., Energy Stor. Mater. 26 (2020) 73.
- [35] J. Chen, X. Fan, Q. Li, Nat. Energy 5 (2020) 386–397.
- [36] I.M. Shlyapnikov, E.A. Goresnik, Z. Mazej, Inorg. Chem. 57 (2018) 1976–1987.
- [37] R. Pathak, K. Chen, A. Gurung, Nat. Commun. 11 (2020) 93.
- [38] X.Q. Zhang, X.B. Cheng, X. Chen, C. Yan, Q. Zhang, Adv. Funct. Mater. 27 (2017) 1605989.
- [39] C. Monroe, J. Newman, J. Electrochem. Soc. 152 (2005) A396–A404.
- [40] Y. Li, A. Pei, Science 358 (2017) 506–510.
- [41] X.B. Cheng, R. Zhang, C.Z. Zhao, Q. Zhang, Chem. Rev. 117 (2017) 10403–10473.
- [42] S.H. Choi, S.K. Park, J.K. Lee, Y.C. Kang, J. Power Sources. 284 (2015) 481–488.
- [43] B.D. Adams, J. Zheng, X. Ren, W. Xu, J.G. Zhang, Adv. Energy Mater. 8 (2018) 1702097.